Efficacy of an external chromia layer in reducing nitridation of high temperature alloys

Corrosion Science 197 (2022) 110050

Contents lists available at ScienceDirect

Corrosion Science

journal homepage: www.elsevier.com/locate/corsci

Efficacy of an external chromia layer in reducing nitridation of high temperature alloys

T. Sand [a,*], S. Bigdeli [b], M. Sattari [c], J. Andersson [d], M. Hättestrand [d], T. Helander [e], J. Eklund [a], J.-E. Svensson [a], M. Halvarsson [c], L.-G. Johansson [a]

[a] Department of Chemistry and Chemical Engineering, Chalmers University of Technology, S-412 96 Gothenburg, Sweden
[b] Swerim AB, S-164 07 Kista, Sweden
[c] Department of Applied Physics, Chalmers University of Technology, S-412 96 Gothenburg, Sweden
[d] Sandvik Materials Technology AB, S-811 81 Sandviken, Sweden
[e] Kanthal AB, S-734 27 Hallstahammar, Sweden

ARTICLE INFO

Keywords:
A. Alloy
B. SEM
B. XRD
B. STEM
C. High temperature corrosion
C. Oxidation

ABSTRACT

Six high temperature alloys have been exposed in N_2/H_2 environments at 900 °C. In order to study the efficacy of a chromia barrier layer against nitrogen ingress, experiments were performed in two environments having the same N_2/H_2 ratio but slightly different water content, chromia formation being spontaneous in one case only. The samples were evaluated by SEM/STEM/EDX, XRD, gravimetry and GD-OES. The presence of an external chromia scale reduced nitridation of the alloy by 50–95%. Furthermore, in the presence of a continuous alumina layer no nitridation of the alloy was detected.

1. Introduction

High-temperature alloys are often used in heat treatment furnace components such as muffle tubes, mesh belts and radiant tubes. In furnaces applying protective low oxygen activity atmospheres containing N_2, the alloys can suffer nitridation. Nitridation can reduce component lifetime since nitride precipitates makes the alloy brittle and depletes the alloy matrix in chromium and aluminum which are needed to form a protective oxide scale.

How prone alloys are to become nitrided depends both on their ability to form a protective oxide scale and on the alloy's intrinsic resistance towards nitrogen pick-up. The formation of protective oxide scales is spontaneous if the oxygen activity in the atmosphere and the activity of chromium, silicon and/or aluminum in the alloy are sufficiently high. At 900 °C the oxygen activity needed to form an oxide scale from the pure elements is 10^{-24}, 10^{-28} and 10^{-37} for chromia, silica and alumina, respectively [1]. If a continuous oxide layer forms on the metal surface, it will present a barrier towards the ingress of nitrogen into the alloy. The effectiveness of that barrier layer depends on its morphology, surface chemistry and transport properties.

While chromia scales are known to be permeable to nitrogen, the mechanism responsible for nitrogen penetration through a continuous chromia layer is not understood [2–4]. Nitrogen penetration is considered to require dissociation of the relatively unreactive N_2 molecule. While the di-nitrogen molecule is reported to dissociate readily on chromia surfaces [3], little is known about how nitrogen is transported through the oxide scale. It has been proposed that nitrogen ingress involves diffusion along oxide grain boundaries, similar to carbon [5]. The transport of nitrogen through a chromia scale is reportedly reduced by a high concentration of water vapor [6].

Chromia-forming alloys often contain silicon and it has been reported that silicon increases the resistance against nitridation [7]. However, the presence of a continuous silica layer in the scale has been shown to increase the tendency for chromia spallation [8].

Alloys forming continuous and adherent alumina scales often feature excellent high temperature corrosion resistance. First-principle calculations have shown that, in contrast to chromia, the alumina surface does not catalyze the dissociation of the N_2-molecule [3]. A recent investigation of the nitridation of two alumina-forming ferritic alloys at 900 °C showed that nitridation only occurred at imperfections in the alumina scale, while the continuous alumina scale was impermeable to nitrogen [9]. Hence, if the alumina scale is discontinuous, allowing nitrogen to access the alloy substrate, severe nitridation may occur.

In the absence of a continuous external oxide layer, the pick-up of

* Corresponding author.
E-mail address: tommy.sand@chalmers.se (T. Sand).

https://doi.org/10.1016/j.corsci.2021.110050
Received 13 October 2021; Received in revised form 22 December 2021; Accepted 23 December 2021
Available online 29 December 2021

nitrogen by the metal is relatively rapid and the rate of nitridation depends on the chemical composition and structure of the alloy. The nitridation rate is then controlled by the diffusion of nitrogen in the alloy and obeys parabolic behavior [10,11]. The solubility and diffusivity of nitrogen in the alloy are determined by alloy composition and crystal structure. The well-known superior ability of Ni-base alloys to resist nitridation compared to Fe-base austenitic alloys [12] has been attributed to the decreasing solubility of nitrogen with increasing nickel content [12,13]. The concentration of chromium in the alloy should also be limited since both solubility and diffusivity of nitrogen increases with rising chromium content [11,14]. Moreover, it is reported that the N_2 molecule adsorbs and dissociates more easily on iron compared to nickel [15] which can influence the pick-up of nitrogen by the alloy.

The only sub-surface nitride identified in previous studies of the nitridation of chromia-forming alloys is Cr_2N [16]. Pure chromium is reported to form a continuous Cr_2N layer in the near-surface region [4,6,16] while chromium containing iron- and nickel based alloys form Cr_2N precipitates in the alloy matrix, often in the form of needles [12,17,18].

The purpose of this study is to analyze how effective chromia scales are in preventing nitrogen ingress into the metal in comparison with the degree of nitrogen pick-up when no scale is present. Therefore, five austenitic alloys able to form chromia scales in sufficient oxygen activity environment were studied in regard to nitrogen permeability through the scale. In addition, the behavior of the chromia-formers are compared to an alumina-forming alloy able to form an alumina scale without macro defects.

2. Materials and experimental

2.1. Materials

The chemical compositions of the alloys investigated are presented in Table 1. The alloys 253 MA, 310H, 800HT, 353 MA and 600 are all austenitic alloys and designed to form chromia scales in environments with sufficient oxygen activity. Both 253 MA and 353 MA contains silicon additions but do not normally form continuous silica layers [19]. Nitrogen is also present in the "MA"-alloys. Small amounts of aluminum and titanium are added to 800HT and 600 in order to increase strength by γ' formation. Kanthal™ EF101 is a FeCrAl alloy designed to form an alumina scale. Silicon is added to this alloy in order to improve oxidation behavior at intermediate temperatures, as reported in [20,21].

Sample coupons with the dimension 15 × 10 × 2 mm were prepared from all alloys except for EF101 where the dimension was 15 × 15 × 2 mm. The coupon faces were prepared by grinding with SiC paper in several steps, with mesh grits ranging from 500# to 4000#. The grinding was followed by polishing with 1 μm diamond paste. The edges of the coupons were only subject to grinding with 1000# mesh grit SiC paper. After grinding and polishing, cleaning was performed in an ultrasonic bath, first in acetone and then in ethanol.

2.2. Experimental setup

The exposures were performed in horizontal tube furnaces equipped with sintered alumina tubes. The environment consisted of 5 vol% H_2 and 95 vol% N_2 with impurity levels of oxygen which are transformed to H_2O at the exposure temperature. The exposures were performed in two environments having different levels of oxygen impurities. The dew points were determined using a Michelle instruments S8000 high-precision chilled mirror hygrometer and were measured to −58.0 ± 1.2 °C, corresponding to 14 ± 2 ppm H_2O, and −48.7 ± 0.2 °C, corresponding to 45 ± 1 ppm H_2O, in the two environments. Using Thermo-Calc Software, the oxygen activity in the two gas environments was calculated to $1.6 * 10^{-23}$ in the environment with 14 ppm H_2O and $1.7 * 10^{-22}$ in the environment with 45 ppm H_2O. Below, the environment with 14 ppm H_2O is designated "environment L" while the 45 ppm case is designated "environment H". Fig. 1 presents an equilibrium diagram for the chromium/nitrogen/oxygen system at 900 °C, showing the thermodynamically stable phases as a function of the activity of oxygen and nitrogen. The two environments L and H are indicated in the diagram, showing that chromia formation is expected in environment H but not in environment L. It should be noted that the diagram is for pure chromium and that for alloys with activity of chromium < 1 there will be a slight shift of the lines towards lower oxygen activities.

Exposures were performed with triplicate samples that were placed in alumina sample holders. Prior to the start of the furnaces, a homogenous environment was obtained by purging the gas mixture for 24 h with an average flow velocity of 9.3 cm/min. After purging, the furnace was started and reached the operating temperature of 900 °C after about 1 h. All exposures lasted 168 h. The samples were left to cool in the furnace, reaching room temperature after about 8 h.

After exposures, mass gains were recorded using a Sartorius™ 6-decimal balance.

2.3. Analysis methods

The samples were analyzed by Scanning Electron Microcopy (SEM) using a Zeiss Ultra 55™ FEG-SEM in 50° tilted- and cross-sectional view with an acceleration voltage of 2 kV. The cross-section samples were prepared by Broad Ion Beam (BIB) milling in a Leica TIC3X™. Selected

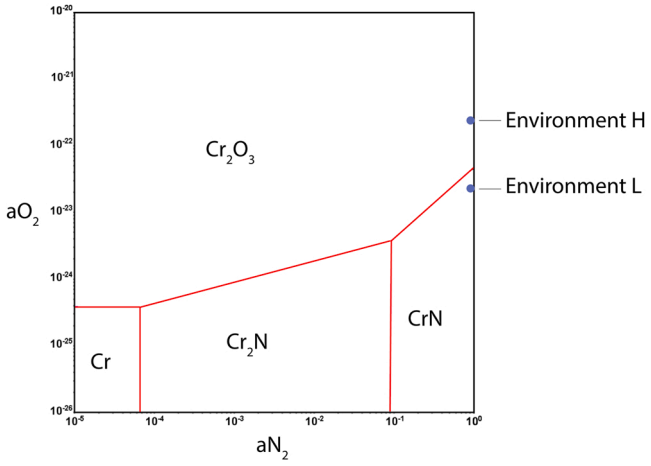

Fig. 1. Equilibrium diagram for the chromium/nitrogen/oxygen system at 900 °C.

Table 1
Chemical composition of tested alloys (wt%).

Alloy	Cr	Al	C	Si	Mn	Ni	N	Fe	Other
253 MA	21.0		0.07	1.52	0.67	10.8	0.156	Bal.	Ce
310H	24.3		0.05	0.34	1.24	20.2	0.038	Bal.	
800HT	20.3	0.46	0.06	0.44	0.50	30.3	0.012	Bal.	Ti
353 MA	25.7		0.07	1.39	1.68	34.9	0.172	Bal.	Ce
600	16.7	0.14	0.01	0.31	0.19	Bal.	0.006	9.8	Ti
EF101	12.4	3.7	0.02	1.25	0.10		0.01	Bal.	RE

samples were further prepared by Focused Ion Beam (FIB) milling using a FEI Versa 3D FIB/SEM to obtain lift-out specimens for further examination by Scanning Transmission Electron Microscopy (STEM) using a Titan 80–300 TEM/SEM equipped with a Schottky Field Emisson Gun (FEG), a C_s-probe corrector and a High Angle Annular Dark Field (HAADF) detector. In addition, Energy Dispersive X-ray Analysis (EDX) was performed using an Oxford X-sight detector.

X-Ray Diffraction (XRD) utilizing Bragg-Brentano geometry was used to identify crystalline phases formed. The instrument was a Bruker D8 ADVANCE equipped with a Cu Kα source.

Chemical depth profiles were obtained by Glow Discharge Optical Emission Spectroscopy (GD-OES) using a Spectruma GDA 750 HR. The technique is characterized by excellent depth resolution and low detection limits. The anode was ring-shaped with 2.5 mm diameter. The instrument was operating at 800 V/15 mA and the samples were sputtered with argon ions. After measuring to the maximum depth, about 50–100 μm, the samples were removed, and the crater was removed by grinding before the measurement was continued. By repeating this step multiple times and adding the consecutive measurements to each other, depth profiles to about 350 μm were obtained.

3. Results

3.1. Microstructure overview

The microstructures of the near-surface regions of the six alloys after 168 h exposure at 900 °C in environment H (95% N_2, 5% H_2, 45 ppm H_2O) are presented in Fig. 2, the upper row showing top view images from a 50° tilted angle, while the bottom row shows cross-sectional views. Fig. 2 shows that chromia layers have formed on the five austenitic alloys while the FeCrAl (EF101) has formed an alumina scale. In addition, the two austenitic alloys with added silicon (253 MA and 353 MA) have formed an inner SiO_2 layer. The silica layer on 353 MA is discontinuous and relatively thick while it is thinner and continuous on 253 MA. Also, the scale outside of the silica layer contains more voids in the case of 253 MA. Limited spallation of the chromia layer was observed for 253 MA (not illustrated). The two alloys with the highest concentration of manganese, 310H and 353 MA, feature blade-like oxide grains at the scale surface containing manganese and chromium. All alloys except EF101 have formed precipitates in the alloy substrate. However, they all feature a precipitation-free zone in the vicinity of the metal/oxide interface (most clearly seen for 353 MA, 800HT and 310H in Fig. 2).

Fig. 3 shows the microstructure of the six alloys after exposure in environment L (95% N_2, 5% H_2, 14 ppm H_2O). In this case, surface oxides are absent on the austenitic alloys, except for 253 MA and 353 MA where discontinuous silica layers are present. The alumina-forming EF101 has formed an oxide scale which is slightly thicker compared to the one formed in environment H. All alloys except EF101 exhibit a high density of precipitates, both at the alloy surface and in the alloy bulk. Comparing Figs. 2 and 3 shows that exposure in environment L resulted in significantly greater amounts of precipitates than environment H. In both environments, precipitation is more extensive at the alloy grain boundaries compared to within the grains.

Table 2 shows the crystalline phases detected by XRD after exposure of the six alloys in the two environments. In environment H, chromia (Cr_2O_3) and spinel oxide (M_3O_4) were detected on all five austenitic alloys. In contrast, the only evidence for crystalline oxides on the austenitic alloys after exposure in environment L are weak diffraction from spinel oxide in the case of 310H, 800HT and 353 MA. Thus, no chromia was detected after exposure in environment L. In the case of the EF101, γ-Al_2O_3 was identified after exposure in both environments. All five austenitic alloys gave evidence for Cr_2N in both environments. In addition, weak diffraction from CrN was observed for 600 after exposure in environment L. All samples showed strong diffraction from the metal matrix (not included in the table).

3.2. Gravimetry

Because volatilization is considered to be negligible and due to the absence of spallation (except a small amount for 253 MA in environment H), the mass gain is simply the sum of the oxygen and nitrogen uptake by the samples. Fig. 4 shows mass gain in the two environments (the Ni-content of the five austenitic alloys increases from left to right in the figure). In environment L, the mass gain of the austenitic alloys decreases with increasing Ni-content. Because oxide formation on the austenitic alloys is quite small in this environment, this trend indicates that nitridation decreases with increasing Ni-content, which is in agreement with the expectations [12]. It is noted that, despite the much greater oxide formation in environment H, four of the five austenitic alloys exhibit lower mass gains in environment H than in environment L. The mass gain corresponding to oxide formation can be calculated from the thickness of the oxide layers, see Figs. 2 and 3 (internal oxidation was negligible). The average thickness of the layers making up the oxide scale was estimated from the SEM cross sections. Scale porosity was disregarded, and the oxide density was put at 5.2 gcm^{-3} for Cr_2O_3, 2.2 gcm^{-3} for SiO_2 and 4.0 gcm^{-3} for Al_2O_3. The calculations only provide estimates of the oxygen uptake since there is some variation in the composition and thickness of the oxide layers. The measured mass gains, the calculated mass gain due to oxide formation and the

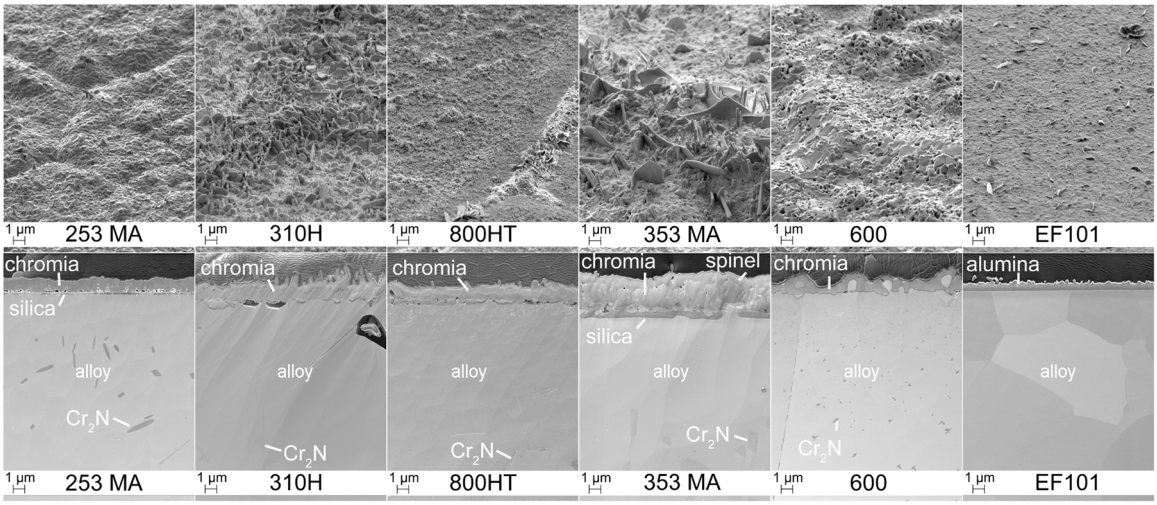

Fig. 2. SEM-SE images showing a 50° tilted top view (top) and cross-sectional view (bottom) of the six alloys exposed at 900 °C in environment H.

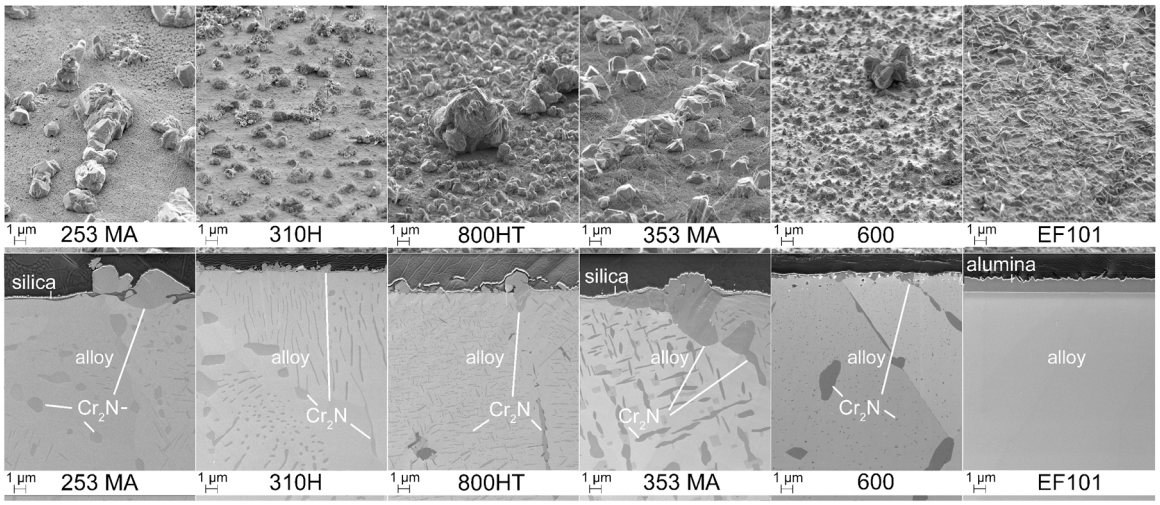

Fig. 3. SEM-SE images showing a 50° tilted top view (top) and cross-sectional view (bottom) of the six alloys exposed at 900 °C in environment L.

Table 2
Crystalline phases observed by XRD after exposure in the two environments.

	chromia	spinel	γ-alumina	CrN	Cr_2N
Environment H					
253 MA	X	X			
310H	X	X			
800HT	X	X			
353 MA	X	X			
600	X	X			
EF101			X		
Environment L					
253 MA					X
310H		X (weak)			X
800HT		X (weak)			X
353 MA		X (weak)			X
600				X (weak)	X
EF101			X		

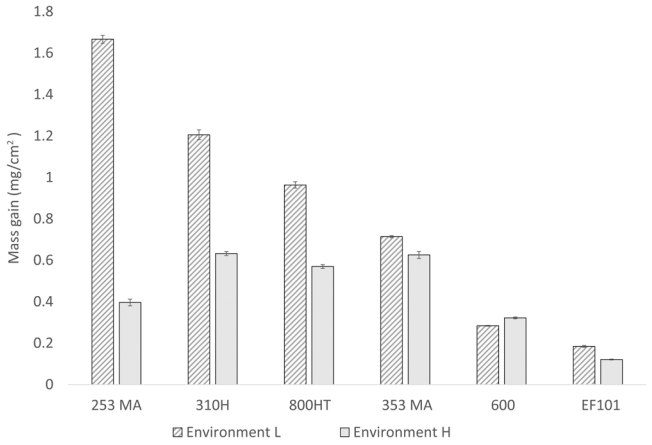

Fig. 4. Mass gains of the six different alloys after exposures for 168 h at 900 °C in environment L and environment H.

calculated net nitrogen pick-up (equal to the mass gain after subtracting the mass of oxygen in the scale) for the six alloys are listed in Table 3. For the alumina-forming alloy, the calculation indicates that, in both environments, the entire mass gain is explained by the formation of the oxide scale. For the five austenitic alloys, the calculation shows that nitrogen pick-up is significantly lower in environment H where chromia formed than in environment L where chromia was absent. The reduction in nitrogen uptake compared to environment L is presented in Table 3. The two alloys 253 MA and 353 MA show reductions of nitrogen pick-up by about 90%, while the three other alloys show reductions of about 65%.

3.3. Nitrogen pick-up measured by GD-OES

The nitrogen levels in the six alloys after exposure in environment L and H were examined by GD-OES. The nitrogen depth profiles are presented in Fig. 5. For all five austenitic chromia-forming alloys, higher nitrogen concentrations are observed after exposure in environment L. This is in agreement both with the calculated nitrogen uptakes in Table 2 and with the analysis of the microstructure in Figs. 2 and 3. Also in agreement with the calculated nitrogen pick-up and the microstructural investigation, the GD-OES analysis showed no nitrogen pick-up by the alumina forming EF101. The degree of reduction of the nitrogen pick-up in environment H as compared to environment L was calculated from the GD-OES curves and is presented in Table 4. The calculation involved integrating the area beneath the nitrogen curve and correcting for the nitrogen content in the alloy bulk as measured by conventional chemical analysis. The results are in good agreement with Table 3. It is noted that the nitrogen uptake measured by gravimetry is 2–4 times larger than the nitrogen uptake estimated by integrating the GD-OES curves. This is believed to be due to a lack of precision in the depth measurement in the latter, meaning that the depth of nitrogen ingress into the alloys in correspondingly greater than indicated by GD-OES. This implies that nitrogen has reached almost 1 mm into the alloys, in fair agreement with the expected diffusion length of nitrogen in austenite at 900 °C which is calculated to 1.8 mm, using D_0 and Q from [22].

3.4. Detailed microstructure

Fig. 6 shows a STEM HAADF-image, including an EDX line scan, of 353 MA exposed in environment H. In accordance with Fig. 3, it shows an oxide scale with a thickness of about 4 μm. The bright surface layer is the protective platinum layer deposited during preparation of the lift-out specimen. The oxide scale is shown to consist of two layers, a manganese-rich outer layer and an inner chromia layer. Based on the EDX line-scan and the identification of spinel oxide by XRD (see Table 2) the outer layer is attributed to $MnCr_2O_4$ spinel. Manganese was also present in the oxide close to the metal interface in a similar way as observed previously [23]. The silica layer is present in the sub-chromia region and beneath a roughly 0.5 μm thick strip of base metal. Its composition is consistent with SiO_2, with no significant impurities. Furthermore, the line-scan shows that the alloy is depleted in chromium, the nominal chromium content of 25 wt% (27 at%) being reduced to

Table 3
Measured mass gain and mass of oxygen in oxide (calculated from the scale thickness) for the six alloys after exposure in the two environments. The nitrogen pick-up equals the mass gain minus the mass of oxygen in the oxide layer. The reduction in nitrogen pick-up by the formation of oxides is also presented.

	Environment L (mg/cm^2)			Environment H (mg/cm^2)			Reduction in nitrogen pick-up in environment H
Alloy	Measured mass gain	Mass of oxygen in oxide	Nitrogen pick-up	Measured mass gain	Mass of oxygen in oxide	Nitrogen pick-up	
253 MA	1.667	0.03	1.64	0.396	0.19	0.21	87%
310H	1.205	0	1.21	0.632	0.22	0.41	66%
800HT	0.963	0	0.96	0.570	0.26	0.31	68%
353 MA	0.713	0.03	0.68	0.626	0.57	0.06	91%
600	0.284	0	0.284	0.322	0.22	0.10	65%
EF101	0.184	0.23	0	0.120	0.13	0	n/a

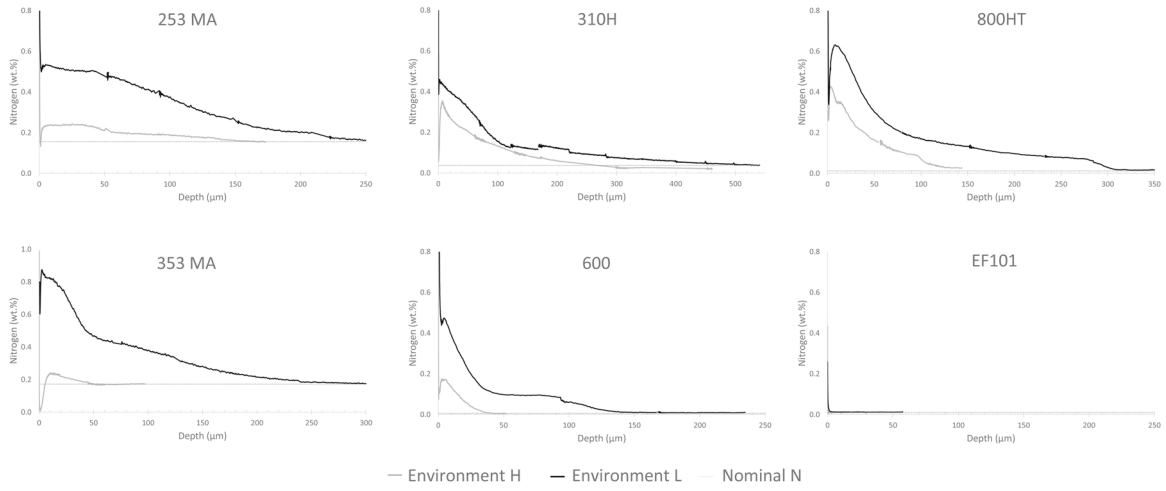

Fig. 5. GD-OES nitrogen depth profiles after exposures in environment H and L at 900 °C plotted together with nominal nitrogen concentration. The absolute depth could be 2–4 times deeper in order to correspond to mass pick-up by gravimetry.

Table 4
Relative reduction of nitrogen pick-up in environment H compared to environment L from GD-OES analysis (Fig. 5).

Alloy	Reduction in nitrogen pick-up measured by GD-OES
253 MA	83%
310H	50%
800HT	61%
353 MA	95%
600	75%
EF101	n/a

about 20 at%. Note that the image only depicts the precipitation-free zone in the alloy (see Fig. 2) and that nitride particles are hence absent.

Fig. 7 shows a STEM HAADF image and an EDX line-scan of alloy 353 MA after exposure in environment L. In accordance with Fig. 3, chromia and spinel layers are absent on the surface. The particle protruding from the alloy surface consists of Cr_2N. Next to it, a bright Pt layer sits on top of a band with dark contrast consisting of silica. About 0.5–1.1 µm beneath the Cr_2N particle, there is an area which is rich in oxygen, manganese and silicon. The stoichiometry from EDX indicates that it could consist of manganese orthosilicate, Mn_2SiO_4. Large amounts of Cr_2N precipitates are present in the alloy substrate. The chromium depletion of the metal matrix in this region is greater than in environment H, the chromium concentration being about 10 at% in this case, as opposed to 20 at% in environment H.

Fig. 8 shows a cross-section SEM-SE image of 253 MA after exposure in environment L for 168 h. In this case, the chromium nitride particle on the metal surface consists of both CrN and Cr_2N, CrN appearing at the nitride/gas phase boundary. The large Cr_2N particle protrudes through a gap in the discontinuous silica layer. All nitrides observed in the substrate where of type Cr_2N.

4. Discussion

The main objective of this study is to investigate the ability of spontaneously formed chromia layers to mitigate the nitridation of high temperature alloys. Thus, while chromia layers are known to be permeable to nitrogen at high temperature, this paper explores whether the presence of a surface chromia layer may still slow down nitrogen ingress enough to impact alloy nitridation significantly. In addition to five chromia-forming austenitic alloys, one alumina-forming FeCrAl alloy is included for comparison.

4.1. Nitridation in environment L

As expected, exposure in environment L, in which the oxygen activity is insufficient for spontaneous formation of chromia (see Fig. 1), resulted in almost oxide-free surfaces on the austenitic alloys, cf. Fig. 3. Thus, the only oxides detected on the surface after exposure were traces of spinel (Table 2) and, in the case of 253 MA and 353 MA, a discontinuous silica layer (see Fig. 2).

The spinel detected by XRD after exposure in environment L is suggested to be $MnCr_2O_4$ which was observed in environment H (see Fig. 6). The layer morphology and the absence of diffraction from crystalline forms of silica indicate that the SiO_2 layers formed in both L and H environments are glasses. This is in accordance with [19] where it is reported that alloy 353 MA forms a discontinuous silica glass sub-scale

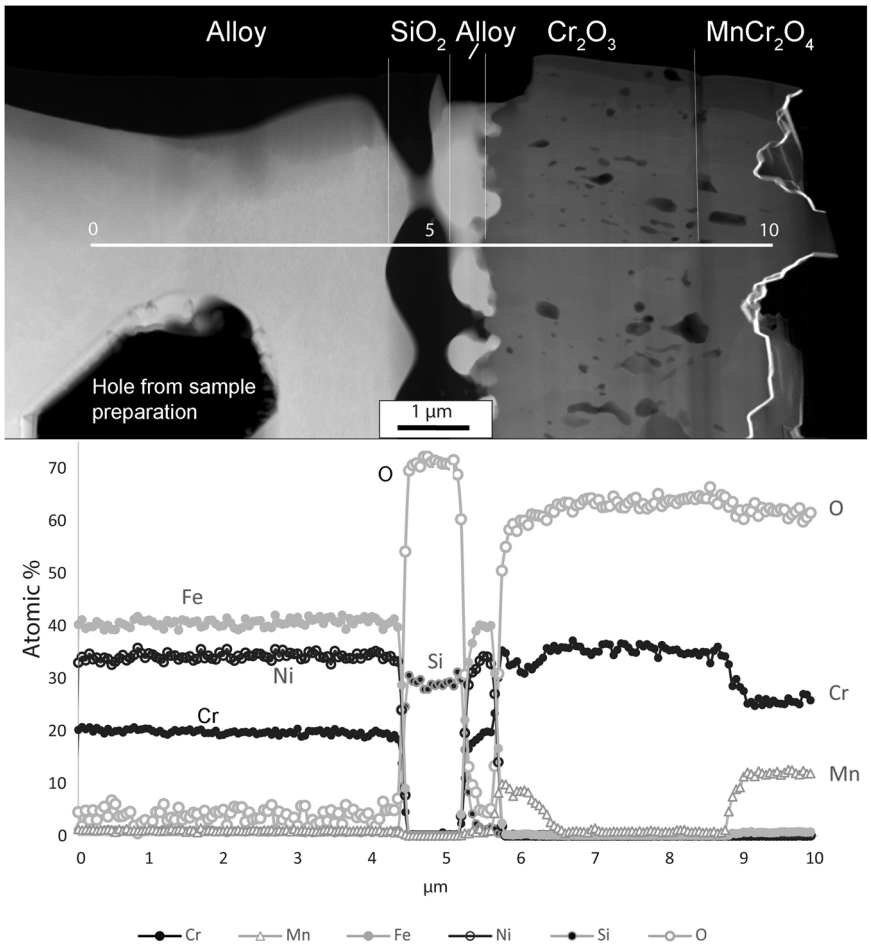

Fig. 6. STEM HAADF image and EDX line-scans showing 353 MA exposed at 900 °C in environment H for 168 h. Note: surface to the right.

during high-temperature oxidation in air. The formation of SiO_2 and $MnCr_2O_4$ in environment L is expected, considering alloy composition and because both compounds are more thermodynamically stable than chromia [1,24].

The thermodynamic data show that the formation of chromium nitride is spontaneous in environment L (see Fig. 1). Accordingly, the alloys exhibit numerous chromium nitride particles, both at the "bare metal" surface and in the alloy substrate (Fig. 3). Which one of the two existing chromium nitrides Cr_2N and CrN, that is stable depends on the activity of nitrogen and chromium, see reactions (1) and (2):

$$Cr_2N(s) + ½N_2(g) \rightleftarrows 2CrN(s) \quad (1)$$

$$Cr_2N(s) \rightleftarrows CrN(s) + Cr(ss) \quad (2)$$

The XRD analysis (Table 3) shows that Cr_2N has formed in both environments (L and H) with weak evidence for CrN only in environment L. Accordingly, SEM/EDX analysis showed that the nitride precipitates in the matrix of the five chromia-forming alloys invariably consisted of Cr_2N (as previously reported [2,16]), while CrN was only detected at the surface, after exposure in environment L. The latter case is illustrated by the SEM-SE image in Fig. 8, showing 253 MA after exposure in environment L. It shows a nitride precipitate at the alloy surface, which consists mainly of Cr_2N, but also exhibits thin CrN regions at the gas/solid interface.

According to the thermodynamic data, CrN is the stable chromium nitride at equilibrium with the experimental gas (Fig. 1). The predominance of Cr_2N hence implies that reaction (1) has not reached equilibrium. This in turn implies that the uptake of nitrogen at the alloy surface is relatively slow in comparison to the flux of nitrogen into the alloy (c.f. the nitrogen gradients in Fig. 5). It should be noted that the CrN observed at the surface (Fig. 7) may have formed during cooling (after exposure), rather than at 900 °C, reaction (1) being shifted towards CrN with decreasing temperature.

It should be noted that the alloy showing the highest nitrogen uptake (253 MA) features a silica layer which covers a large part of the surface but is not completely continuous. This implies that the silica scale by itself is not very effective in protecting against nitrogen ingress, in agreement with previous studies [25].

In the absence of a continuous chromia oxide scale, the rate of nitridation and nitrogen uptake depends on alloy properties. It is well-known that alloys with high nickel content are more resistant against nitridation [12], the effect being attributed to a lower solubility of nitrogen in the alloy matrix [13]. The same trend was observed in the present study, the extent of nitridation was decreasing with the nickel content. Calculations by Thermo-Calc (using TCFE10) gives the following solubility of nitrogen in the matrix at 900 °C: 253 MA = 0.023; 310H = 0.018; 800HT = 0.0089; 353 MA = 0.0033 and 600 = 0.0024 giving the same trend as the observed nitrogen pick-up.

4.2. Nitridation in environment H – the effect of the chromia layer on nitridation

Comparing the microstructures and nitrogen profiles of the five chromia-forming alloys after exposure in the two environments shows that the continuous chromia/Cr-Mn spinel layers formed in environment H are accompanied by a significant decrease in nitrogen uptake and a change in the distribution of nitride precipitates (cf., Figs. 2, 3, 5, Tables 3 and 4). It should be pointed out that the two sets of experiments

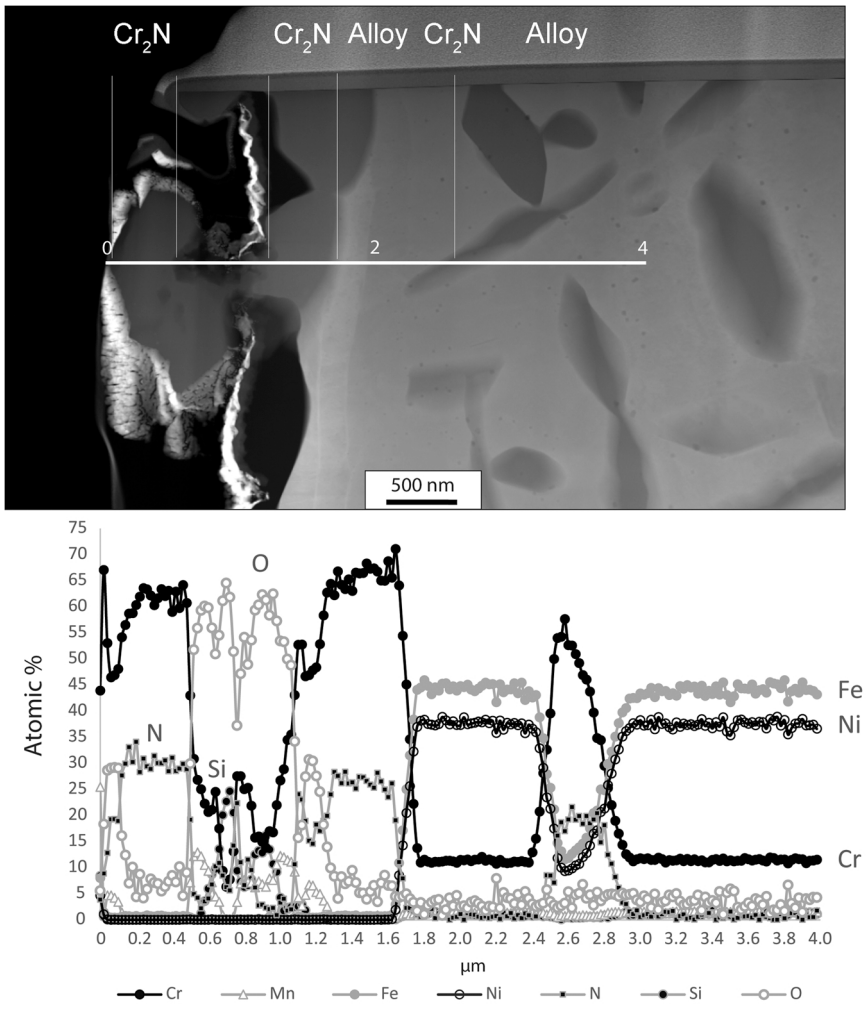

Fig. 7. STEM HAADF image and EDX line-scans showing 353 MA exposed at 900 °C in environment L for 168 h. Note: surface to the left.

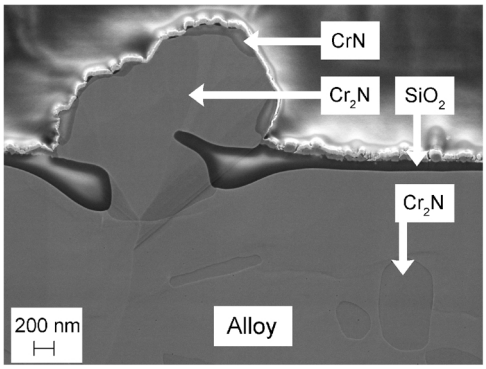

Fig. 8. SEM-SE image showing 253 MA exposed at 900 °C in environment L for 168 h.

are identical, except for the concentration of water vapor, which is high enough for the formation of a chromia layer in environment H (45 ppm) but not in environment L (14 ppm). It is hence concluded that the 50–95% reduction in the uptake of nitrogen by the five alloys in environment H (Tables 3 and 4) can be attributed to the presence of the external chromia layers.

In the absence of an external oxide layer, the uptake of nitrogen from the experimental gas starts by the adsorption and dissociation of N_2 molecules on the metal surface. The nitrogen atoms then enter the metallic solid solution and diffuse into the alloy substrate and react with chromium, forming chromium nitride precipitates. The presence of a continuous surface oxide adds more steps to the nitridation process. Thus, the initial adsorption and dissociation of N_2 must now happen on the top surface of the oxide layer (in our case Cr-Mn spinel oxide or chromia). The subsequent transport of nitrogen across the oxide layer to the metal is likely in the form of nitride ions (N^{3-}) because of the ionic nature of the oxide layer. When it has been transported across the chromia layer, the nitrogen species must react again at the metal/oxide interface in order to enter the metal. The deceleration of alloy nitridation by the surface chromia layer, evidenced in this study, can be due to any of these processes. However, in view of the well-known ability of transition metal surfaces (i.e., iron) to catalyze the dissociation of the kinetically very stable N_2 molecule, it is likely that the reduced nitridation rate is at least partly due to slow dissociation of N_2 on the oxide surface.

The current study shows both that the chromia layer mitigates alloy nitridation and that it is permeable to nitrogen. To investigate the kinetics of the permeation process, time-resolved studies are necessary. The process itself, including interface reactions and transport processes, may be addressed both by theory and by experiment. Thus, trapped nitrogen in, e.g., oxide grain boundaries can be detected with instruments having atomic resolution.

Tables 3 and 4 show that for alloys 310H, 800HT and 600, the presence of a chromia layer reduces nitrogen uptake by 50–75%, while the reduction is 83–95% for 253 MA and 353 MA. It is suggested that this reflects a real difference in the ability of the oxide scales on the two

groups of alloys to protect against nitrogen ingress. It is noted that while alloys 253 MA and 353 MA both formed a silica sub-scale beneath the chromia layer (Figs. 2 and 6), the oxide scales on the three other alloys did not contain silica. This suggests that the presence of a silica layer (discontinuous for 353 MA and continuous for 253 MA) beneath the chromia layer enhances the ability of the oxide scale to protect against nitrogen ingress. As noted above, the silica surface layer formed in environment L appears to have little effect on nitridation. The mechanism behind the protectiveness of the combined silica/chromia scale will be subject to further study.

4.3. Nitride morphology

The two sets of experiments resulted in distinct differences in the morphology and density of nitride precipitates. In environment L precipitates appear both at the surface and in the interior of the alloy. For the two silica-forming alloys the nitrides at the surface are fewer and larger compared to the other three chromia-formers. In environment H, the alloy immediately beneath the oxide scale exhibits a precipitation-free zone. It is proposed that this is because of chromium depletion due to the formation of the surface chromia layer. In both environments, nitride precipitation is favored in the alloy grain boundaries, which is expected due to their higher defect density. It should be noted that Cr_2N precipitation seems to follow preferred orientations in the substrate matrix.

4.4. The alumina-forming alloy

Figs. 2 and 3, and Tables 3 and 4, show that the alumina-forming FeCrAl alloy EF101 is far superior to the other five alloys in resisting nitridation under these conditions. This is in accordance with Mortazavi et. al [9] who reported that the alumina scales studied were in general excellent barriers towards nitrogen, nitridation only occurring at certain scale imperfections. In the present study, no nitridation was observed in the alumina-forming alloy. The microscopic overview images and gravimetry both indicate that the alumina layer has grown somewhat thicker in environment L than in environment H. That difference will not be discussed here as it is outside the scope of this paper. It is emphasized that the present comparison between alumina and chromia layers relates to a specific set of conditions and that, e.g., thermal cycling can cause cracking of alumina scales which, can allow direct reaction of N_2 with the substrate, canceling any advantage of the alumina scale per se.

It is suggested that the inherently excellent ability of alumina scales to protect against alloy nitridation is related, partly to its continuous nature and partly to surface properties. Thus, Geers et al. [3] reports that the N_2 molecule is unable to dissociate on an alumina surface in the temperature range of interest.

5. Conclusions

- The nitridation of five austenitic Fe- and Ni-base alloys in N_2+H_2 environment at 900 °C was reduced 50–95% by a spontaneously formed external Cr_2O_3 layer.
- The greatest reduction of nitridation was observed for two alloys which also formed a silica sub-scale, beneath the chromia layer.
- The extent of nitridation decreased with increasing Ni-content in the alloys.
- The nitrogen precipitates in the alloy bulk consisted of Cr_2N.
- In the absence of a surface chromia layer both Cr_2N and CrN formed on the metal surface.
- The FeCrAl alloy EF101 formed continuous alumina scales and showed no sign of nitridation.

CRediT authorship contribution statement

T. Sand: Methodology, Investigation, Writing – original draft, Visualization. **S. Bigdeli:** Data curation, Writing – review & editing. **M. Sattari:** Formal analysis. **J. Andersson:** Formal analysis, Writing – review & editing. **M. Hättestrand:** Conceptualization, Funding acquisition. **T. Helander:** Conceptualization, Funding acquisition, Writing – review & editing. **J. Eklund:** Formal analysis, Writing – review & editing. **J.-E. Svensson:** Conceptualization, Funding acquisition, Supervision, Writing – review & editing. **M. Halvarsson:** Conceptualization, Writing – review & editing. **L.-G. Johansson:** Conceptualization, Funding acquisition, Supervision, Writing – review & editing, Project administration.

Declaration of Competing Interest

The authors declare that they have no known competing financial interests or personal relationships that could have appeared to influence the work reported in this paper.

Data availability

The raw/processed data required to reproduce these findings cannot be shared at this time due to technical or time limitations.

Acknowledgments

This work was carried within the Swedish High Temperature Corrosion Centre (HTC) at Chalmers University of Technology. Sandvik Materials Technology is acknowledged for supplying materials and performing GD-OES measurements.

References

[1] B. Gleeson, 1.09 – thermodynamics and theory of external and internal oxidation of alloys, in: B. Cottis (Ed.), Shreir's Corrosion, Elsevier, Oxford, 2010, pp. 180–194.
[2] X.G. Zheng, D.J. Young, High temperature reaction of chromium with multi-oxidant atmospheres, in High Temperature Corrosion and Protection of Materials 4, Pts 1 and 2, R. Streiff, et al., Editors, 1997, pp. 567–574.
[3] C. Geers, et al., Properties of alumina/chromia scales in N-2-containing low oxygen activity environment investigated by experiment and theory, Oxid. Met. 87 (3–4) (2017) 321–332.
[4] K. Taneichi, et al., Oxidation or nitridation behavior of pure chromium and chromium alloys containing 10 mass% ni or Fe in atmospheric heating, Mater. Trans. 47 (10) (2006) 2540–2546.
[5] D.J. Young, et al., Penetration of protective chromia scales by carbon, Scr. Mater. 77 (2014) 29–32.
[6] M. Michalik, et al., Effects of water vapour on the high temperature nitridation of chromium, Mater. Corros.-Werkst. Und Korros. 65 (3) (2014) 260–266.
[7] A. Soleimani-Dorcheh, M.C. Galetz, Oxidation and nitridation behavior of Cr-Si alloys in air at 1473 K, Oxid. Met. 84 (1–2) (2015) 73–90.
[8] H.E. Evans, et al., Influence of silicon additions on the oxidation resistance of a stainless steel, Oxid. Met. 19 (1) (1983) 1–18.
[9] A.N. Mortazavi, et al., Exploring failure modes of alumina scales on FeCrAl and FeNiCrAl alloys in a nitriding environment, Acta Mater. 201 (2020) 131–146.
[10] L.E. Kindlimann, G.S. Ansell, Kinetics of internal nitridation of austenitic Fe-Cr-Ni-Ti alloys, Metall. Trans. 1 (1) (1970) 163.
[11] H.J. Christ, S.Y. Chang, U. Krupp, Thermodynamic characteristics and numerical modeling of internal nitridation of nickel base alloys, Mater. Corros.-Werkst. Und Korros. 54 (11) (2003) 887–894.
[12] K. Tjokro, D.J. Young, Comparison of internal nitridation reactions in ammonia and in nitrogen, Oxid. Met. 44 (3–4) (1995) 453–474.
[13] H.A. Wriedt, O.D. Gonzalez, The solubility of nitrogen in solid iron-nickel alloys near 1000-degrees-C, Trans. Metall. Soc. Aime 221 (3) (1961) 532–535.
[14] S.Y. Chang, , U. Krupp, H.J. Christ, The influence of thermal cycling on internal oxidation and nitridation of nickel-base alloys, in Cyclic Oxidation of High Temperature Materials: Mechanisms, Testing Methods, Characterisation and Life Time Estimation, M. Schutze and W.J. Quadakkers, Editors, 1999, pp. 63–81.
[15] C.J.H. Jacobsen, et al., Catalyst design by interpolation in the periodic table: bimetallic ammonia synthesis catalysts, J. Am. Chem. Soc. 123 (34) (2001) 8404–8405.
[16] M.P. Brady, P. Sachenko, Effects of Fe on the oxidation/internal nitridation behavior and tensile properties of Cr and oxide dispersion ductilized Cr, Scr. Mater. 52 (9) (2005) 809–814.
[17] U. Krupp, H.J. Christ, Internal nitridation of nickel-base alloys. Part II. Behavior of quaternary Ni-Cr-Al-Ti alloys and computer-based description, Oxid. Met. 52 (3–4) (1999) 299–320.
[18] M. Auinger, E.M. Muller-Lorenz, M. Rohwerder, Modelling and experiment of selective oxidation and nitridation of binary model alloys at 700 degrees C – the systems Fe, 1 wt%{Al, Cr, Mn, Si}, Corros. Sci. 90 (2015) 503–510.

[19] T. Jonsson, et al., Influence of H2O(g) on the oxide microstructure of the stainless steel 353MA at 900 degrees C in oxygen, J. Electrochem. Soc. 154 (11) (2007) C603–C610.
[20] J. Eklund, et al., The influence of silicon on the corrosion properties of FeCrAl model alloys in oxidizing environments at 600 degrees C, Corros. Sci. 144 (2018) 266–276.
[21] T. Sand, et al., Exploring the effect of silicon on the high temperature corrosion of lean FeCrAl alloys in humid air, Oxid. Met. 95 (3–4) (2021) 221–238.
[22] W.F. Gale, T.C. Totemeier, Smithells Metals Reference Book, Elsevier, 2003.
[23] H. Falk-Windisch, J.E. Svensson, J. Froitzheim, The effect of temperature on chromium vaporization and oxide scale growth on interconnect steels for Solid Oxide Fuel Cells, J. Power Sources 287 (2015) 25–35.
[24] H. Kurokawa, K. Kawamura, T. Maruyama, Oxidation behavior of Fe–16Cr alloy interconnect for SOFC under hydrogen potential gradient, Solid State Ion. 168 (1) (2004) 13–21.
[25] R. Jargelius-Pettersson, et al., Nitrogen uptake by austenitic stainless steels on annealing in N2–H2 atmospheres, Mater. Sci. Technol. 9 (12) (1993) 1123–1132.